Applied Physics B (2023) 129:191
https://doi.org/10.1007/s00340-023-08136-2

Applied Physics B
Lasers and Optics

RESEARCH

Enhancing laser-driven proton acceleration using a lithium target

M. Turki[1] · O. Culfa[2] · D. Bennaceur-Doumaz[3]

Received: 5 December 2022 / Accepted: 27 October 2023 / Published online: 23 November 2023

Abstract
Laser–plasma acceleration of ions has been of interest for the past few decades. An effective way to enhance laser-driven proton acceleration is to improve laser absorption in plasmas. In this study, we show that lithium (Li) is the most promising candidate for accelerating protons with better absorption among target light weight materials used for ion acceleration. For this, two-dimensional particle-in-cell (PIC) simulations were performed to investigate the acceleration of ions and protons with a high-power laser (with an amplitude a_0=10 and a pulse duration of 30 fs) to determine the optimal lithium target thickness for maximum energies. The maximum energy of Li ions is achievable with a target thickness of 40 nm, while the maximum proton energy can be achieved for a 30nm thickness of the target. Moreover, a series of PIC simulations were also performed with targets of different atomic numbers and thicknesses to understand lithium's performance for the acceleration of protons. Compared to other targets, such as Al (Aluminum), C (Carbon), and Be (Beryllium), the Li target has a significant enhancement in proton energy, which can be used as an alternative target to enhance proton and ion energies in future experiments.

1 Introduction

Ion acceleration via laser–matter interactions has been a leading research topic, since the first experiments were conducted in the 1980s [1]. With rapid advancements in ultra-intense laser technology, lasers are now able to focus on targets with intensities exceeding 10^{18}Wcm^{-2} and accelerate particles with energies reaching tens or hundreds of MeV [1–3]. This area has gained considerable interest because of its potential applications in hadron therapy [4], materials processing [5], materials characterization [6], radiography [7], and high-energy density physics [8], among others. Proton beams with energies of more than 200 MeV and energy spreads less than 0.1%, as well as approximately 10^{10} protons per second, are necessary for a proton beam to be used in hadron therapy [9].

Accelerating ion beams with high-power lasers is possible via several ion acceleration mechanisms, such as Target Normal Sheath Acceleration (TNSA) [10], Radiation Pressure Acceleration (RPA) [11], Break-Out Afterburner (BOA) [12], and Shock Wave Acceleration (SWA) [13]. Through the different acceleration mechanisms, strong electric fields are generated from electron displacement by a laser. These electric fields, which arise from the separation of space charges, accelerate ion beams directly (TNSA, RPA, and BOA) or create shock waves capable of reflecting and trapping plasma ions (SWA).

There are many unique properties of these beams, including high luminance, short duration, and low emittance. TNSA is considered one of the most well-established and robust mechanisms for ion acceleration in linear polarization (LP) with moderate laser intensities ($> 10^{18}$Wcm^{-2}). During this mechanism, ions and protons are accelerated from the rear surface of the target by a strong electric sheath field created by fast electrons, which are accelerated at the front surface of the target. The energy and temperature of the hot electrons were found to be key parameters in the process.

The optimum acceleration regime has been determined through the continuous investigation of both laser parameters and target thicknesses. One of the most important laser parameters is the pulse duration that has been reduced over the years from the picosecond level to femtoseconds (20–30

✉ M. Turki
mturki@usthb.dz

[1] Radiation Physics Department, Faculty of Physics, University of Science and Technology Houari Boumediene, BP 32, El Alia, Bab Ezzouar, 16111 Algiers, Algeria

[2] Department of Physics, Karamanoglu Mehmetbey University, 70200 Karaman, Turkey

[3] Centre de Développement des Technologies Avancées, Cité 20 Août 1956, Baba, Hassen, 16081 Algiers, Algeria

fs) made possible by the Chirped Pulse Amplification (CPA) technique [14]. It was demonstrated that the energy spectrum of accelerated ions and protons could be controlled by appropriately choosing the target thickness and by adding a hydrogen layer on the rear side of the target [15, 16]. Accelerating ions to high energies is not possible with a laser pulse unless a driving electron effect to efficiently transfer energy between the laser and the ions is present. It has been found that the maximum energy of the accelerated protons is proportional to the temperature of the hot electrons as $E_{\text{proton}} \approx \beta T_{\text{hot}}$, where β is a constant [1]. Previous experimental and theoretical studies show that hot electrons can be produced via several mechanisms from the irradiated front side of the target with collisional heating such as inverse bremsstrahlung [17] and collisionless heating such as resonance absorption [18], vacuum heating [19], and ponderomotive acceleration [20] depending on the laser and target parameters [21]. The collision effect is negligible when $I\lambda^2 > 10^{16}$ W cm^{-2} μm^2, where λ is the laser wavelength. In the intensity range, 10^{18} W cm^{-2} μm^2 $> I\lambda^2 > 10^{16}$ W cm^{-2} μm^2, and at oblique polarization of the laser, resonance absorption and vacuum heating are concurrent mechanisms of absorption; depending on the pre-plasma density scale length L. In fact, when the plasma scale length L is very steep, $L << \lambda$, vacuum heating prevails, while resonance absorption occurs if L is large enough. At the laser intensity greater than 10^{18} Wcm^{-2} μm^2 and for a plasma scale length comparable to λ, the absorption mechanism is dominated by ponderomotive heating [22].

In addition, heavier ions than protons can be used for other purposes besides cancer therapies, such as generating nuclear reactions, synthesizing heavy elements, and producing biomedical isotopic compounds [23].

The present work is focused on the effect of lithium (Li) target on proton acceleration using 2D EPOCH-PIC code [24] simulations and a comparison to other commonly used elements in laser–plasma experiments, especially light ones, has been addressed. Li is an element of particular interest due to the requirement for accelerated lithium ions to initiate nuclear reactions [25, 26], as well as the higher energy of the protons produced by this target compared to targets made from heavier elements. Petrov and Davis [27] studied light ion acceleration computationally with similar elements with target thicknesses of 0.1–10 μm, a preformed exponential scale length, and irradiances of 10^{18}–10^{22}W/cm^2, with pulse durations of 10–1000 fs. They found that Li^{+3} is the element with the best conversion efficiency for the 1 μm target compared with C^{+6} and Al^{+13}. Our study is mainly focused on proton acceleration and the effect of other materials on the acceleration process and energy; in addition to ion acceleration with a target of sub-micron thickness without preformed scale length (since we assumed that the laser has a high-contrast ratio). In this study, 2D EPOCH-PIC simulations were used to determine how the energy of lithium ions and protons evolves with a lithium target thickness ranging from 20 nm to 1μm. In order to achieve this, a laser pulse with an amplitude of $a_0 = 10$ and a pulse duration of 30 fs was selected, and a lithium target was used with a rear surface layer of hydrogen and a step-like density profile. For targets of thickness $\lesssim$ 1 μm, the intensity achieved during pre-pulse irradiation must be below the ionization threshold (~ 10^{11}–10^{13} Wcm^{-2}) to not affect the integrity of the target or ionize it before the arrival of the main laser pulse [28]. The proton energy obtained with the lithium target is compared to those obtained from targets made of other elements.

2 Simulation setup

Our simulations have been performed in two-dimensional (2D) geometry using the PIC code EPOCH [24]. The simulation domain size was 80 μm × 30 μm in the x–y-direction with a mesh resolution of 8000 × 3000, corresponding to a cell size of 10 nm. The target is placed at 30 μm along the x-axis.

The laser was linearly polarized and struck the target at normal incidence, which was along the x-axis. We have employed a laser pulse with an irradiance of $I = 2.14 \times 10^{20}$Wcm^{-2} corresponding to a normalized vector potential $a_0 = eE_0/m_e\omega c \approx 10$, where E_0 is the initial laser electric field amplitude,e is the electron charge, m_e is the electron mass, ω is the laser frequency, and c is the speed of light. The laser had a wavelength $\lambda = 800$ nm, a pulse duration of 30 fs, and a 5 μm focal spot size, and a power of 168 TW.

We designed a target of Li with a 20 nm hydrogen layer on the rear surface. We assumed the initial density of Li is 0.534 g/cm^3, and the target is initially fully ionized. Each simulation cell is filled with 64 electrons, 64 Li^{3+} ions, and 100 protons. The ion and electron densities were set to $27n_c$ and $81n_c$, respectively, where $n_c \cong 1.72 \times 10^{21}$ cm^{-3} represents the critical density deduced from the relation: $n_c = \varepsilon_0 m_e \omega^2/e^2$, where ε_0 is the dielectric constant in the vacuum. Since very high-intensity laser pulses were used, we assumed that the plasma was fully ionized when the laser pulse interacted with the target. The effect of collisions was also neglected as the plasma quickly heated to electron temperatures of the order of hundreds of keV. We assumed also that the laser had a high contrast and, therefore, no pre-plasma was created before the interaction with the main pulse. In fact, using a pre-pulse of high magnitude can destroy targets with thicknesses in nm before the arrival of the main pulse, and then, the study of particle acceleration can be affected [29]. We used open boundary conditions for the fields and particles to eliminate reflections. The Li target thickness was varied from 20 to 1000 nm with a step-like

density profile. In the second part of the work, where we studied the material effect on proton acceleration, we kept the laser parameters constant and ran the same simulations for Li, Be, C, and Al for target thicknesses of 40, 100, and 400 nm, assuming fully ionized plasma.

3 Results and discussion

3.1 Optimum thickness of lithium target

It is well known that the maximum proton and ion energies decrease as target thickness increases (regardless of the target material), i.e. the maximum energy passes through an optimum, and then decreases as target thickness increases [30, 31]. Several simulations [32–34] and experiments [30, 35, 36] have shown that very thin (sub-micrometer to nanometer-scale) targets can provide higher proton energy and greater conversion efficiency when the laser contrast is sufficiently high to prevent the target from being damaged by the laser pulse. Furthermore, laser–plasma absorption is more efficient on ultra-thin targets due to target decompression, which allows more efficient volume heating of electrons, thereby achieving higher proton beam energy [37]. The maximum energies of Li^{+3} ions and protons for target thicknesses (varying from 20 to 1000 nm) are reported in Fig. 1, which shows the optimum size of the target is 40 nm for maximum energy of Li^{3+} ions and 30 nm for the protons maximum energy. For these optima, the energy of ions and protons is about 3 times higher than that of the 1000 nm-thick target.

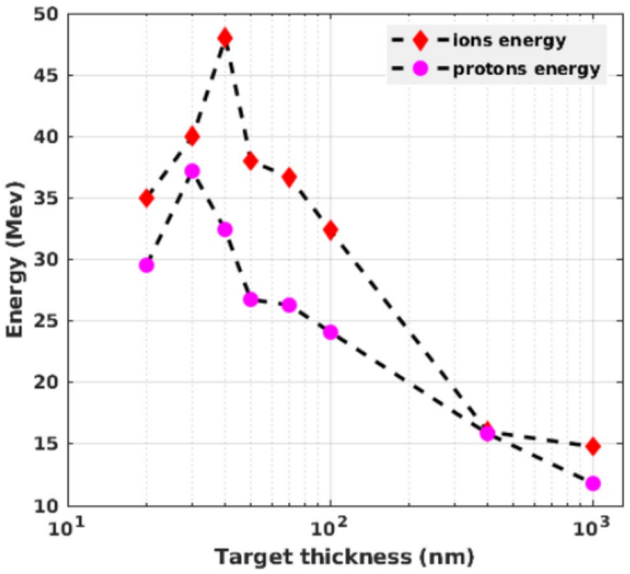

Fig. 1 The maximum energy of Li^{+3} ions and protons as a function of target thickness

When the target thickness is lower than the optimum of 40 nm or 30 nm for maximum ion lithium and proton energies, respectively, the plasma becomes transparent and the laser can pass through the plasma with high absorption and low reflection. In this region of ultra-thin targets, as the thickness increases, the production of energetic electrons responsible of ion acceleration increases proportionally to the thickness of the target, and then, the ion and proton energies increase. This process occurs up to the optimum thicknesses.

Above the optima, the target becomes opaque to the laser whose energy will be increasingly reflected as the target thickness increases. The charge separation potential and the highest energy of ions are then reduced [38].

3.2 Acceleration mechanisms

The temporal evolutions of the electron density (normalized to relativistic critical density) $n_e/\gamma n_c$ (blue) and the laser electric field E_y (red) for 40 and 1000 nm-thick Li target, respectively, where γ is the Lorentz factor, are shown in Figs. 2 and 3. During the early stage time ($t = 160$ fs), the laser interacts with an overdense plasma where $n_e > \gamma n_c$. Starting at 200 fs, the plasma density decreases due to the relativistic effect and turns to transparent, so the target reaches the condition of Relativistically Induced Transparency (RIT) ($n_e < \gamma n_c$) as reported in Fig. 2. Hence, relativistic electron motion causes the plasma to become transparent to the laser and a portion of the laser pulse propagates through the target.

Ion acceleration in the relativistic transparency region [39–41] generally occurs via several stages. Initially, the TNSA mechanism is responsible for the ion acceleration, because the electrons accelerated by the laser traverse to the rear side. In the first phase of this mechanism, ions gain modest energies, following that, an enhanced TNSA phase occurs. In this phase, the laser field heats the background electrons to high temperatures, which reduces the plasma frequency ω_p due to the increase on the electron's relativistic mass. The target expands due to heating, resulting in the electron density decrease, further reducing ω_p, which helps the laser penetrate deeper into the target and creates the BOA mechanism. Then, the electrons are volumetrically heated and boost the longitudinal electric field. In the BOA mechanism, non-linear processes due to the increase of electromagnetic instabilities enhance the energy coupling in the ions [12]. RIT is crucial to observe the BOA mechanism [42].

Figure 3 shows the laser electric field (E_y) and the electron density (n_e) for a 1000 nm thick Li target. During the interaction, the plasma remains overdense and the dominant ion acceleration mechanism is TNSA. As described in the TNSA mechanism, the laser accelerates electrons to higher energies, which subsequently propagate and circulate within the target. The relativistic electrons escape from the target,

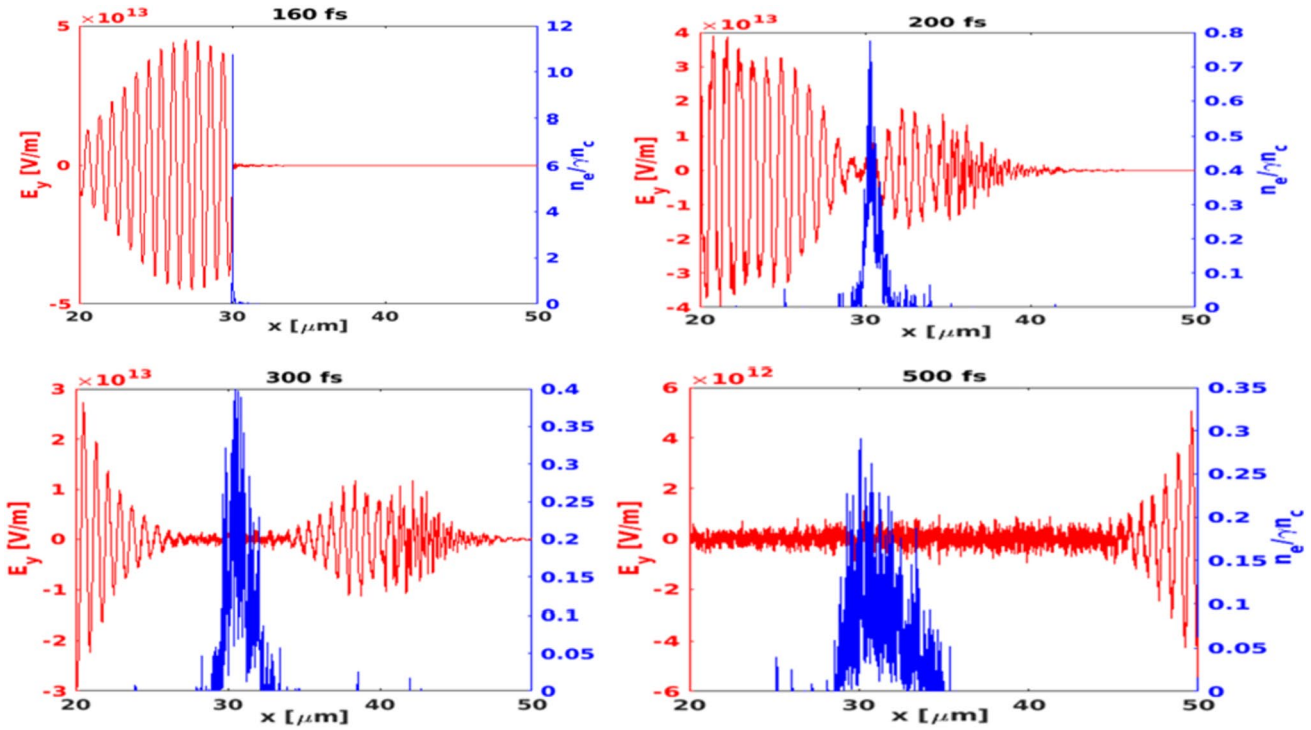

Fig. 2 Temporal evolution of laser electric field (E_y) in red color and plasma electron density to the relativistic critical density ($n_e/\gamma n_c$) in blue color for 40 nm thick Li target

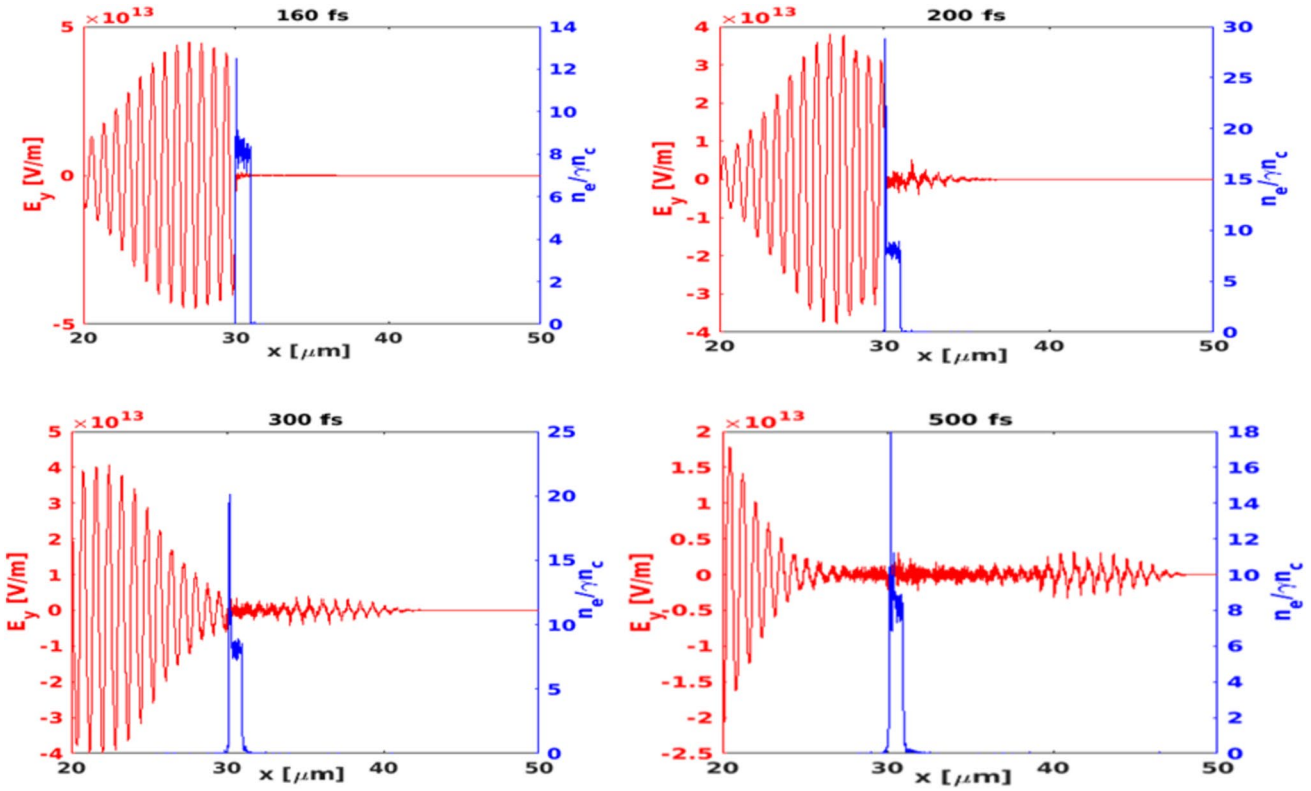

Fig. 3 Temporal evolution of laser electric field (E_y) in red color and plasma electron density to the relativistic critical density ($n_e/\gamma n_c$) in blue color for 1000 nm thick Li target

leaving a positive charge density toward which the remaining hot electrons turn. These electrons re-circulate through the target, generating the necessary electric field for ion and proton acceleration from the target rear side. The longitudinal spatial extent of this charge separation is defined as the Debye length, $\lambda_D = \left(\frac{k_B T_e}{4\pi n_e e^2}\right)^{1/2}$, where k_B is the Boltzmann constant, T_e is the electron temperature, and n_e is the electron density. The TNSA mechanism is important at intensities of around $\sim 10^{18} - 10^{20}$ Wcm^{-2}, while for higher irradiances (>10^{21} Wcm^{-2}) and for circular polarization, the RPA mechanism is on the process. In the latter, the laser exerts a radiation pressure force on the target and the particles propagate ballistically and gain more energy directly from the laser beam more efficiently compared to TNSA. It is effective for short pulses (<100 fs) with ultra-thin (sub-micron) targets and requires very small laser pre-pulse.

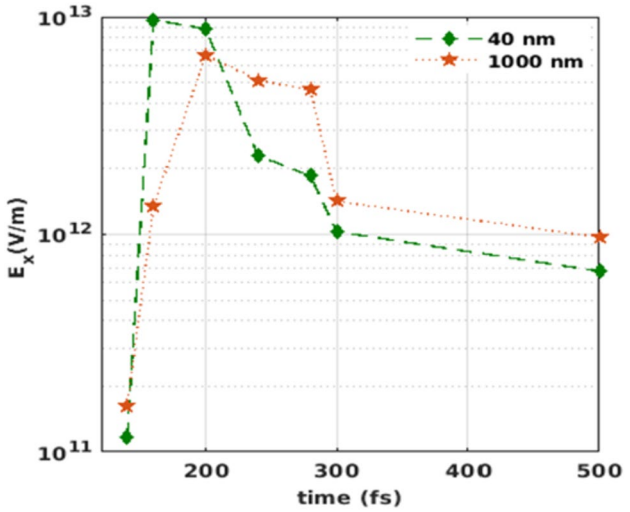

Fig. 4 Temporal evolution of the peak field E_x (V/m) for different thicknesses of Li target

We have also plotted the peak field strength of E_x (V/m) with time for 40 and 1000 nm thick Li target. Figure 4 shows that for a 1000 nm-thick Li target, the sheath field increases at late stages and reaches its maximum at 200 fs, because E_x is enhanced after the electron displacement, whereas for the 40 nm Li target, this field increases at the earlier stages. When we compare the evolution of the maximum electric field at 160 fs, we find the latter enhances by a factor of 7.2 for 40 nm-thick target compared to the electric field from 1000 nm as shown by Fig. 4. This enhancement could be caused by the BOA mechanism [12, 43, 44] when the target becomes partially transparent to the laser pulse.

Figure 5 represents that the energy spectra of Li^{+3} ions, protons, and forward accelerated electrons for different target thicknesses. Here, we notice that the maximum energy for Li^{3+} ions is reached up to 50 MeV for 40 nm thickness, while it is around 15 MeV for thicker targets (> 400 nm). It is also noticed that protons follow the same trend as Li^{+3} ions. However, for 40 nm target, proton energies are reached up to 32 MeV, while the maximum proton energy is only 10 MeV for 1000 nm due to the TNSA mechanism. The latter is responsible for accelerating ions on thick targets. For the thinner target, however, the increase in ion and proton energy is primarily caused by the transparency mechanism. We can also see that electrons can be accelerated up to 40 MeV energies with a 40 nm thick target, while they can be accelerated up to 20 MeV energies with a 1000 nm thick Li target.

3.3 Low Z material effect on proton acceleration

3.3.1 Effect of initial density on proton acceleration

To study the material effect on the energy of the accelerated protons, we performed a series of simulations with different elements and target thicknesses. The obtained proton energy spectra from Li, Be, C, and Al targets are compared

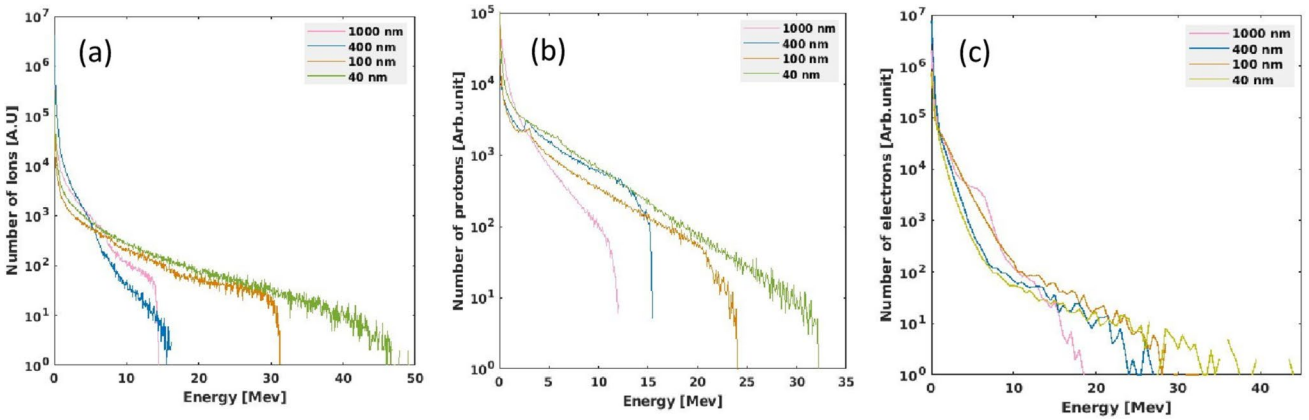

Fig. 5 Energy spectra for Li^{+3} ions (**a**), protons (**b**), and electrons (**c**), for different thicknesses of the target

by keeping the simulation parameters constant. The plasma properties, which are used for the simulations, are listed in Table 1.

Figure 6 shows the evolution of the maximum proton energy versus target material ρ through the atomic number Z. We observe that the maximum proton energy decreases with increasing initial target density and target thickness and that lithium provides the highest proton energy among the considered materials, regardless of target thickness. For the same target thickness, using lower density target materials can obtain a higher proton maximum energy.

The initial density and thickness of the targets affect the behavior of electrons and ions within the plasma and then the formation of the acceleration sheath fields in the target normal direction [45]. We can explain this phenomenon by the electron stopping power as presented by Tayyab et al. [46] in their work on the role of target material in proton acceleration from thin foils irradiated by ultrashort laser pulses. In fact, the electron stopping power refers to the ability of a material to slow down or stop the motion of fast-moving electrons. It depends on various factors, including the density of the target material. Higher density targets have a greater number of particles per unit volume, resulting in a higher stopping power. In other words, denser materials lead to a more significant reduction in the kinetic energy of fast electrons and stop a large fraction of fast electrons population from reaching the target rear. Hence, for these targets, the effective sheath field will be weaker, which consequently results in lower proton energy. On the other hand, in lower density targets and lower atomic number Z, fast electrons can penetrate deeper into the target before experiencing significant energy loss. This can lead to reduced electron stopping power in lower density targets compared to higher density targets, and then, the sheath field is stronger by the increasing of the electron density of the hot electrons at the rear target.

It follows that when a high-energy laser interacts with low-Z materials, a significant quantity of hot electrons with high energy and temperature can be generated. This trend is consistent with our simulation results, as shown in the Fig. 11. These relativistic electrons are able to carry a

Table 1 Target materials used in the simulation: Atomic number Z, density of the material ρ, atomic mass M, ion density n_i, and electron density n_e

Material	Li	Be	C	Al
Z	3	4	6	13
ρ (g cm^{-3})	0.534	1.848	2	2.7
M (a.u)	6.94	9.012	12.01	26.98
n_i (10^{22} cm^{-3})	4.63	12.3	10.02	6.02
n_e (10^{22} cm^{-3})	13.89	49.2	60.12	78.26

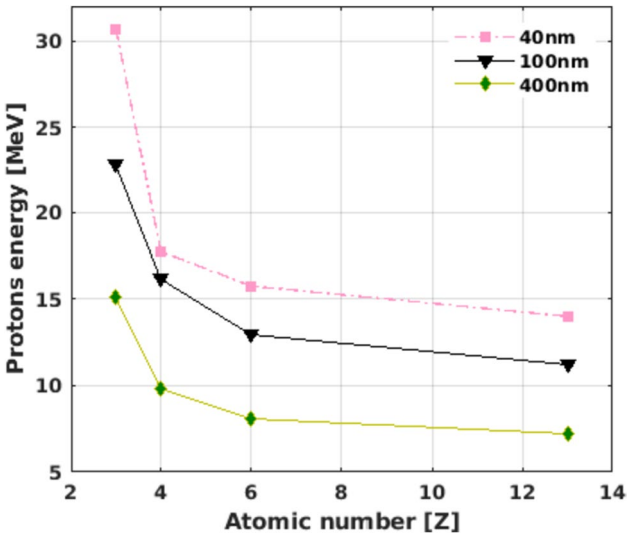

Fig. 6 Maximum proton energy as a function of the atomic number Z for different thicknesses

significant amount of energy, and their temperatures much higher than the surrounding plasma. That can explain the production of higher energy of the protons with lithium target.

A literature review also shows that at given laser intensity, the dependence of the proton maximum energy from the target thickness and electron density is reduced to a dependence on the product of target density and thickness, also called electron areal density [47, 48]. In Fig. 7, we have plotted maximum proton energy as a function of

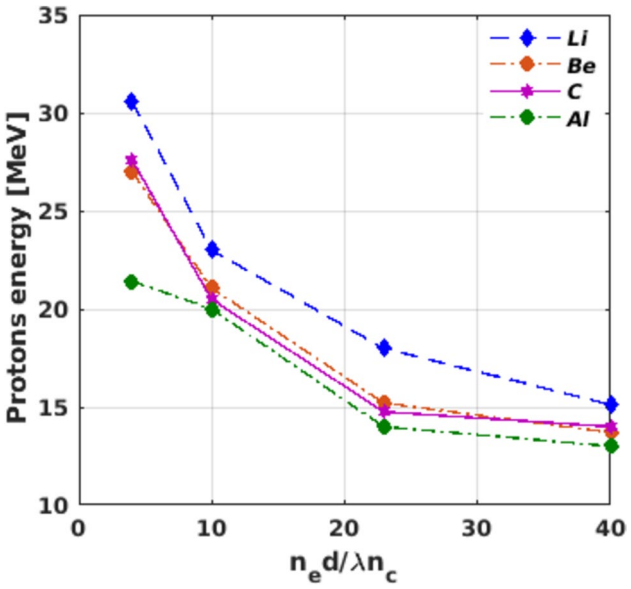

Fig. 7 Maximum proton energy as a function of electron areal density for different materials: Li, Be, C, and Al

dimensionless electron area density $\sigma = \frac{n_e d}{n_c \lambda}$ for the different target materials, where d is the target thickness and n_e is the electron density.

For each electron plasma density relative to the target material, there is an optimum target thickness for which the proton energy gain is the highest. This is illustrated by the lowest value of σ in the figure. This optimal value of areal target density corresponds to a transition between different regimes of ion acceleration, namely TNSA to RIT or BOA, defines transparency of all the targets and maximizes the gained proton energy.

Interestingly, we found in this figure that lithium produces the greatest energy of protons comparatively to the other studied elements, for each areal density up to its optimum. Our previous conclusions are supported by this last finding, since Li presents the best possibility of accelerating protons among the light elements.

Figure 8 shows the energy spectra of protons from various targets with different thicknesses at time $t = 500$ fs. Here, we notice a significant enhancement of the maximum proton energy from Li target which is about a factor of 2, compared to other targets Be, Al, and C for 40 nm thickness, due to a larger number of energetic electrons induced in the acceleration process.

3.3.2 Conversion efficiency from laser to particles

Our simulation results have given laser conversion efficiency to protons up to 6% with lithium target, and it is as low as 2% with aluminum target as shown in Fig. 9. The higher absorption of the laser energy helps to accelerate more hot electrons in Li target compared to the other targets, which

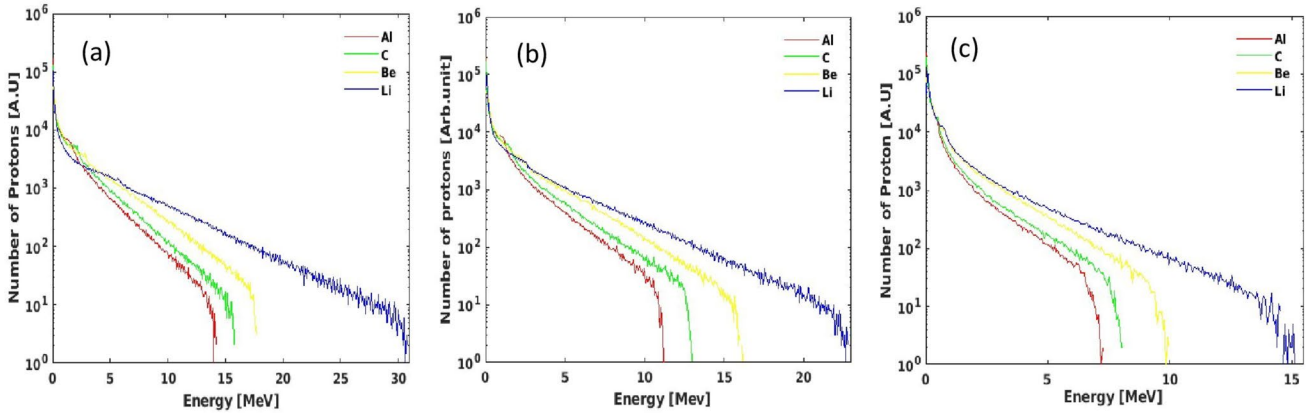

Fig. 8 Energy spectra of protons from different materials: Li, Be, C, and Al for different thicknesses **a** 40 nm, **b** 100 nm, and **c** 400 nm

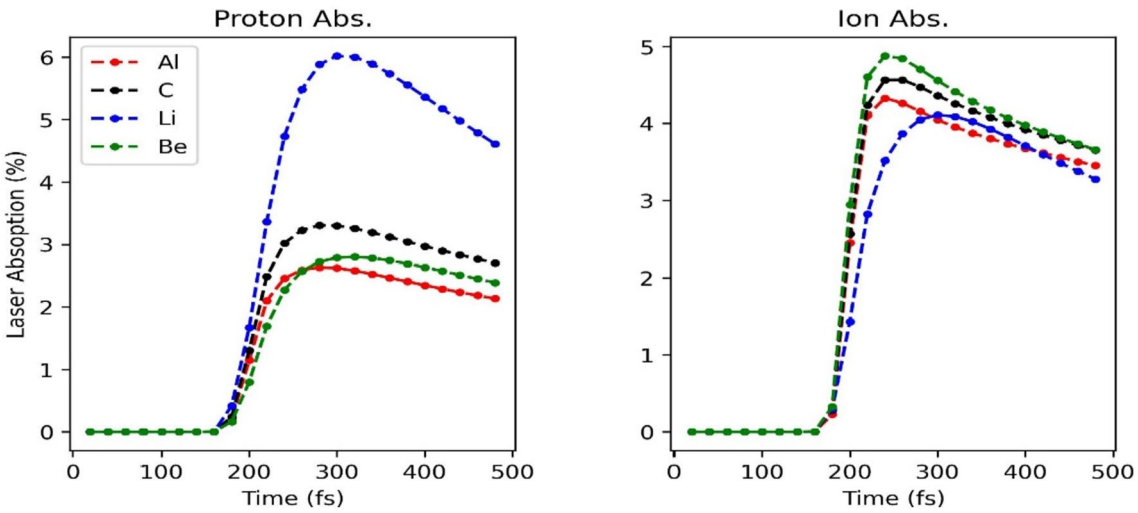

Fig. 9 Temporal evolution of laser conversion efficiency into protons and ions from different target materials; Li (blue), Be (green), C (black), and Al (red) for 40 nm target thickness

can enhance the generation of relativistic electrons at the front side of the target. These electrons are able to reach the rear side fastly and can be re-circulated more, which helps to reinforce the sheath at the rear side of the target, generates more energetic protons. On the other hand, we obtain that the maximum laser energy converted into ions is 4% for lithium, 4.25% for aluminum, 4.5 % for carbon, and about 5% for beryllium (Fig. 9).

It is noteworthy that our 2D PIC simulations only provide a qualitative understanding of the physical processes involved. Compared to 3D PIC simulations and experiments [49, 50], our 2D simulations study give more importance to ion cut-off energy, the conversion efficiency, and hot electrons temperature. Therefore, a quantitative comparison of our results with experimental values is not straightforward. To confirm this, we performed 3D EPOCH simulations for the conversion efficiency into protons and ions as indicated in Fig. 10, which gives lower values than 2D simulations (2.75% instead of 6% for protons and about 2.4 instead of 4.7 for ions). Large energy conversion into protons can be explained via BOA acceleration mechanism, which is the dominant ion acceleration mechanism only with lithium target. The laser penetration observed only with Li target, while there was no penetration through the 40 nm target of the other materials. Note that when transparency occurs, the plasma reflectivity $R(\omega)$ drops substantially [51].

3.3.3 Energy distribution of the hot electrons

Hot electron energy and temperature measurements are needed to determine the maximum proton energy, which is proportional to the temperature of the hot-electron generation in the plasma $E_{\text{proton}} \approx \beta\, T_{\text{hot}}$ [1]. In the theory of the interaction of a femtosecond laser pulse with overdense plasma, the electrons heated by collisionless mechanisms are called "hot" as their kinetic energy is much higher than the energy of thermal electrons named "cold". Because of a high relaxation time of hot electrons compared to the plasma expansion time, two-temperature electron distribution is usually assumed in the plasma initially after the interaction.

Using the EPOCH-PIC simulation code, Fig. 11 shows the energy distributions of hot electrons for different target materials and thicknesses at $t = 200$ fs. They have been used to determine the equivalent electron temperatures of the plasma $k_B T_e$ (Boltzmann energy distributions). Their slopes show the existence of two temperatures for cold and hot electrons inside the plasma, for each target thickness. For 40 nm thickness, estimated cold and hot temperature is about 912 keV and 6 MeV for aluminum, 920 keV and 6 MeV for carbon, 1.21 and 6.67 MeV for lithium, and 1.48 and 6.08 MeV for beryllium targets. In addition, it is observed that electrons from aluminum, carbon, and beryllium have maximum energies of 30 MeV, while electrons from lithium have maximum energy of 35 MeV. Increasing target thickness results in a decrease in the energy obtained by hot electrons and more laser absorption, Li target produces more hot electrons than other elements (Al, C, and Be).

4 Conclusion

In conclusion, we first described the results obtained during the interaction of a high-power laser with a lithium target for different thicknesses, using 2D PIC simulation. While studying the effect of different target thicknesses from 20 to 1000 nm, we have found that there are two optimum target thicknesses (~ 40 and 30 nm) for Li^{+3} ions and protons energy, respectively. In addition, we have seen that the particles are accelerated via two mechanisms TNSA and BOA, depending on the thickness of the Li target. The ion energy increases by a factor of 3 for the 40 nm-thick target compared to the 1000 nm thick target. Secondly, we performed a series of

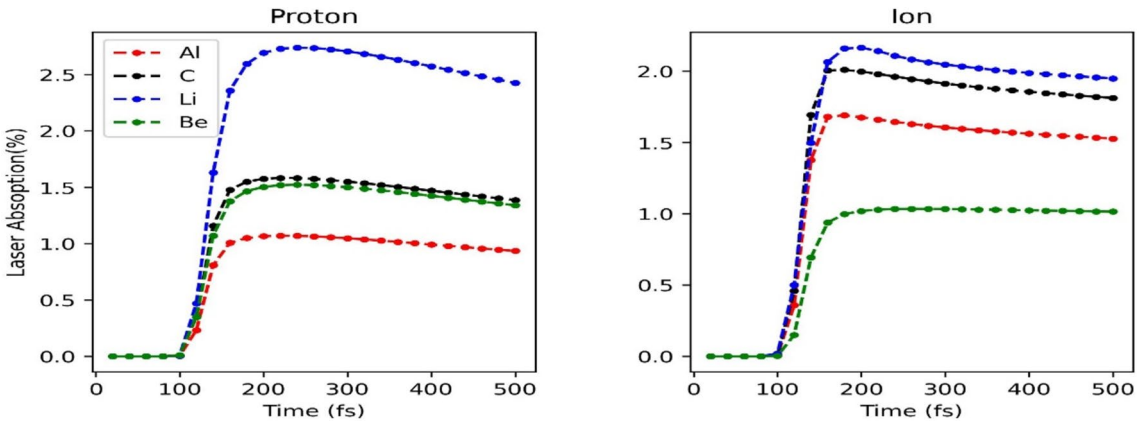

Fig. 10 3D PIC simulation of energy conversion efficiency of laser to protons and ions from different target materials; Li (blue), Be (green), C (black), and Al (red) for 40 nm thickness

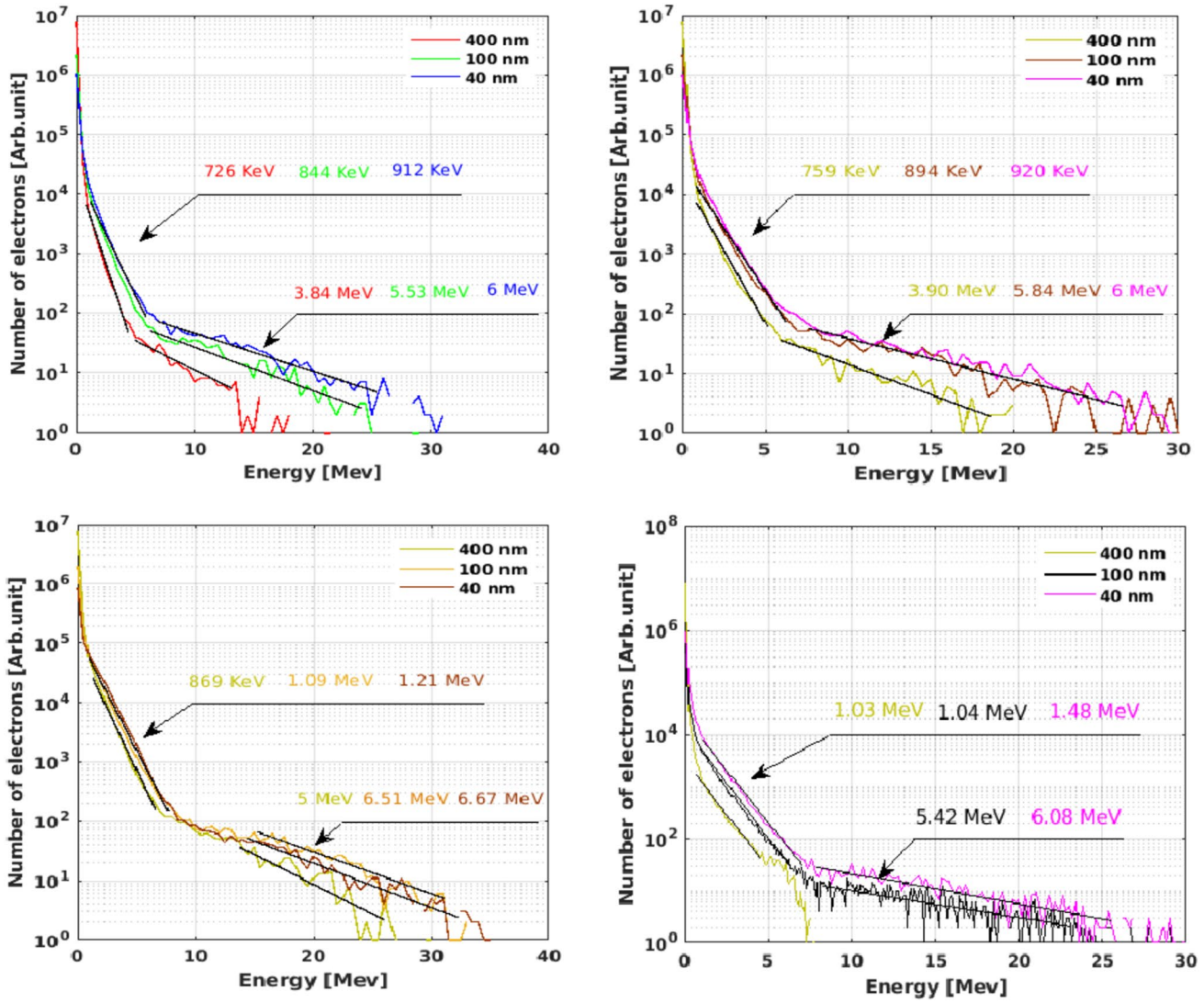

Fig. 11 Energy distribution of the hot electrons from aluminum (top left), carbon (top right), lithium (bottom left), and beryllium (bottom right) targets for different target thicknesses at time $t = 200$ fs

simulations using various elements and target thicknesses. We demonstrated that lithium provides the highest proton energy among the considered materials, regardless of target thickness. In addition, we showed that the lithium target produced more hot electrons with higher energy and the laser can transfer sufficient energy into protons, indicating that lithium has a better absorption than the other targets.

Our findings should lead to a new path to significantly extend the cut-off energy of protons, using lithium as an alternate target for future experiments.

Acknowledgements The authors sincerely thank M. Kumar for valuable comments and for the manuscript editing. Additionally, the authors express our gratitude to Sarah North for proofreading. The EPOCH simulation studies of this work was in part funded by the UKEPSRC grants EP/G054950/1, EP/G056803/1, EP/G055165/1 EP/M018156/1, and EP/ M022-463/1.

Author contributions M.T. conceived of the presented idea, performed the computations, prepared figures and wrote the manuscript with support from O.C. O.C. reviewed the manuscript and contributed to results interpretations. D.B.D. reviewed the manuscript.

Data availability Data are available from the corresponding author upon reasonable request.

Declarations

Conflict of interest The authors declare no competing interests.

References

1. M. Almassarani, B. Beleites, F. Ronneberger, G.G. Paulus, A. Gopal, Plasma **4**, 670 (2021)
2. G. Costa, L. Torrisi, Radiat. Eff. Defects Solids **174**, 11 (2019)

3. S.S. Bulanov, V.Y. Bychenkov, V. Chvykov, G. Kalinchenko, D.W. Litzenberg, T. Matsuoka, A.G.R. Thomas, L. Willingale, V. Yanovsky, K. Krushelnick, A. Maksimchuk, Phys. Plasmas **17**, 043105 (2010)
4. S.S. Bulanov, A. Brantov, V.Y. Bychenkov, V. Chvykov, G. Kalinchenko, Med. Phys. **35**, 1770 (2008)
5. X.P. Zhu, L. Ding, Q. Zhang, Y. Isakova, Y. Bondarenko, A.I. Pushkarev, M.K. Lei, Laser Part. Beams **35**, 587 (2017)
6. M. Passoni, F.M. Arioli, L. Cialfi, D. Dellasega, L. Fedeli, A. Formenti, A.C. Giovannelli, A. Maffini, F. Mirani, A. Pazzaglia, A. Tentori, D. Vavassori, M. Zavelani-Rossi, V. Russo, Plasma Phys. Control. Fusion **62**, 014022 (2019)
7. M. Borghesi, D.H. Campbell, A. Schiavi, M.G. Haines, O. Willi, A.J. MacKinnon, P. Patel, L.A. Gizzi, M. Galimberti, R.J. Clarke, F. Pegoraro, H. Ruhl, S. Bulanov, Plasma Phys. **9**, 2214 (2002)
8. B.Y. Sharkov, D.H.H. Hoffmann, A.A. Golubev, Y. Zhao, Matter Radiat. Extremes **1**, 28 (2016)
9. K.W.D. Ledingham, P.R. Bolton, N. Shikazono, C.-M. Charlie Ma, Appl. Sci. **4**, 402 (2014)
10. S.C. Wilks, A.B. Langdon, T.E. Cowan, M. Roth, M. Singh, S. Hatchett, M.H. Key, D. Pennington, A. MacKinnon, R.A. Snavely, Phys. Plasmas **8**, 542 (2001)
11. T. Esirkepov, M. Borghesi, S.V. Bulanov, G. Mourou, T. Tajima, Phys. Rev. Lett. **92**, 175003 (2004)
12. L. Yin, B.J. Albright, B.M. Hegelich, K.J. Bowers, K.A. Flippo, T.J.T. Kwan, J.C. Fernández, Phys. Plasmas **14**, 056706 (2007)
13. Z. Lécz, A. Andreev, Phys. Plasmas **22**, 043103 (2015)
14. D. Strickland, G. Mourou, Opt. Commun. **56**, 219 (1985)
15. V.T. Tikhonchuk, Nucl. Instrum. Methods Phys. Res. A **620**, 1 (2010)
16. O. Culfa, G.J. Tallents, M.E. Korkmaz, A.K. Rossall, E. Wagenaars, C.P. Ridgers, C.D. Murphy, N. Booth, D.C. Carroll, L.A. Wilson, K.L. Lancaster, N.C. Woolsey, Laser Part. Beams **35**, 58 (2017)
17. M. Moll, M. Schlanges, T. Bornath, V.P. Krainov, New J. Phys. **14**, 065010 (2012)
18. K. Estabrook, W.L. Kruer, Phys. Rev. Lett. **40**, 42 (1978)
19. F. Brunel, Phys. Rev. Lett. **59**, 52 (1987)
20. S.C. Wilks, W.L. Kruer, M. Tabak, A.B. Langdon, Phys. Rev. Lett. **69**, 1383 (1992)
21. O. Culfa, G.J. Tallents, A.K. Rossall, E. Wagenaars, C.P. Ridgers, C.D. Murphy, R.J. Dance, R.J. Gray, P. McKenna, C.D.R. Brown, S.F. James, D.J. Hoarty, N. Booth, A.P.L. Robinson, K.L. Lancaster, S.A. Pikuz, A.Y. Faenov, T. Kampfer, K.S. Schulze, I. Uschmann, N.C. Woolsey, Phys. Rev. E **93**, 043201 (2016)
22. Y.-Q. Cui, W.-M. Wang, Z.-M. Sheng, Y.-T. Li, J. Zhang, Plasma Phys. Control. Fusion **55**, 085008 (2013)
23. J. Braenze, A.A. Andreev, K. Platonov, M. Klingsporn, L. Ehrentraut, W. Sandner, M. Schnürer, Phys. Rev. Lett. **114**, 124801 (2015)
24. T.D. Arber, K. Bennett, C.S. Brady, A. Lawrence-Douglas, M.G. Ramsay, N.J. Sircombe, P. Gillies, R.G. Evans, H. Schmitz, A.R. Bell, Plasma Phys. Control. Fusion **57**, 113001 (2015)
25. S. Ikeda, M. Okamura, T. Kanesue, D. Raparia, A. Hershcovitch, K. Yip, K. Takahashi, A. Cannavò, G. Ceccio, Rev. Sci. Instrum. **91**, 023304 (2020)
26. A. Cannavò, K. Takahashi, M. Okamura, G. Ceccio, T. Kanesue, S. Ikeda, Rev. Sci. Instrum. **91**, 033317 (2020)
27. G.M. Petrov, J. Davis, Appl. Phys. B **96**, 773 (2009)
28. P. McKenna, F. Lindau, O. Lundh, D. Neely, A. Persson, C.-G. Wahlström, Philos. Trans. R. Soc. A **364**, 711 (2003)
29. R.C. Shah, R.P. Johnson, T. Shimada, K.A. Flippo, J.C. Fernandez, B.M. Hegelich, Opt. Lett. **34**, 2273 (2009)
30. D. Neely, P. Foster, A. Robinson, F. Lindau, O. Lundh, A. Persson, C.-G. Wahlström, P. McKenna, Appl. Phys. Lett. **89**, 021502 (2006)
31. D.C. Carroll, O. Tresca, R. Prasad, L. Romagnani, P.S. Foster, P. Gallegos, S. Ter-Avetisyan, J.S. Green, M.J.V. Streeter, N. Dover, C.A.J. Palmer, C.M. Brenner, F.H. Cameron, K.E. Quinn, J. Schreiber, A.P.L. Robinson, T. Baeva, M.N. Quinn, X.H. Yuan, Z. Najmudin, M. Zepf, D. Neely, M. Borghesi, P. McKenna, New J. Phys. **12**, 045020 (2010)
32. T. Esirkepov, Phys. Rev. Lett. **96**, 105001 (2006)
33. K.N. Kim, K. Lee, M. Kumar, H.-N. Kim, S.H. Park, Y.U. Jeong, N. Vinokurov, Y.G. Kim, Phys. Plasmas **23**, 033119 (2016)
34. M. Kumar, K. Lee, H.-N. Kim, W.-J. Ryu, S.H. Park, Y.U. Jeong, AIP Adv. **9**, 045304 (2019)
35. P. Antici, J. Fuchs, E. d'Humières, E. Lefebvre, M. Borghesi, E. Brambrink, C.A. Cecchetti, S. Gaillard, L. Romagnani, Y. Sentoku, T. Toncian, O. Willi, P. Audebert, H. Pépin, Phys. Plasmas **14**, 033102 (2007)
36. T. Ceccotti, A. Levy, H. Popescu, F. Reau, P. D'Oliveira, P. Monot, J.P. Geindre, E. Lefebvre, P. Martin, Phys. Rev. Lett. **99**, 18 (2007)
37. S. Fourmaux, S. Buffechoux, B. Albertazzi, D. Capelli, A. Lévy, S. Gnedyuk, L. Lecherbourg, P. Lassonde, S. Payeur, P. Antici, H. Pépin, R.S. Marjoribanks, J. Fuchs, J.C. Kieffer, Phys. Plasmas **20**, 013110 (2013)
38. Q.L. Dong, Phys. Rev. E **68**, 026408 (2003)
39. A. Henig, D. Kiefer, K. Markey, D.C. Gautier, K.A. Flippo, S. Letzring, R.P. Johnson, T. Shimada, L. Yin, B.J. Albright, K.J. Bowers, J.C. Fernández, S.G. Rykovanov, H.-C. Wu, M. Zepf, D. Jung, V.K. Liechtenstein, J. Schreiber, D. Habs, B.M. Hegelich, Phys. Rev. Lett. **103**, 045002 (2009)
40. J.C. Fernández, D. Cort Gautier, C. Huang, S. Palaniyappan, B.J. Albright, W. Bang, G. Dyer, A. Favalli, J.F. Hunter, J. Mendez, M. Roth, M. Swinhoe, P.A. Bradley, O. Deppert, M. Espy, K. Falk, N. Guler, C. Hamilton, B.M. Hegelich, D. Henzlova, K.D. Ianakiev, M. Iliev, R.P. Johnson, A. Kleinschmidt, A.S. Losko, E. McCary, M. Mocko, R.O. Nelson, R. Roycroft, M.A. Santiago Cordoba, V.A. Schanz, G. Schaumann, D.W. Schmidt, A. Sefkow, T. Shimada, T.N. Taddeucci, A. Tebartz, S.C. Vogel, E. Vold Glen, A. Wurden, L. Yin, Phys. Plasmas **24**, 56702 (2017)
41. A. Higginson, R.J. Gray, M. King, R.J. Dance, S.D.R. Williamson, N.M.H. Butler, R. Wilson, R. Capdessus, C. Armstrong, J.S. Green, S.J. Hawkes, P. Martin, W.Q. Wei, S.R. Mirfayzi, X.H. Yuan, S. Kar, M. Borghesi, R.J. Clarke, D. Neely, P. McKenna, Nat. Commun. **9**, 724 (2018)
42. J. Strehlow, D. Kawahito, M. Bailly-Grandvaux, F.N. Beg, G.M. Petrov, Plasma Phys. Control. Fusion **63**, 065011 (2021)
43. B.M. Hegelich, I. Pomerantz, L. Yin, H.C. Wu, D. Jung, B.J. Albright, D.C. Gautier, S. Letzring, S. Palaniyappan, R. Shah, K. Allinger, R. Hörlein, J. Schreiber, D. Habs, J. Blakeney, G. Dyer, L. Fuller, E. Gaul, E. Mccary, A.R. Meadows, C. Wang, T. Ditmire, J.C. Fernandez, New J. Phys. **15**, 085015 (2013)
44. D. Sangwan, O. Culfa, C.P. Ridgers, S. Aogaki, D. Stutman, B. Diaconescu, Laser Part. Beams **37**, 1 (2019)
45. L.N. Su, B. Liu, X.X. Lin, F. Liu, F. Du, X.L. Liu, Y. Zheng, X.L. Ge, Y.T. Li, Z.M. Sheng, L.M. Chen, W.M. Wang, J.L. Ma, X. Lu, Z.Y. Wei, J.E. Chen, J. Zhang, Sci. China-Phys. Mech. Astron. **56**, 457 (2013)
46. M. Tayyab, S. Bagchi, B. Ramakrishna, T. Mandal, A. Upadhyay, R. Ramis, J.A. Chakera, P.A. Naik, P.D. Gupta, Phys. Rev. E **90**, 023103 (2014)
47. T. Esirkepov, M. Yamagiwa, T. Tajima, Phys. Rev. Lett. **96**, 105001 (2006)
48. H. Daido, M. Nishiuchi, A.S. Pirozhkov, Rep. Prog. Phys. **75**, 056401 (2012)
49. S. Sinigardi, J. Babaei, G. Turchetti, Nucl. Instrum. Methods Phys. Res. A **909**, 438 (2018)
50. L. Fedeli, A. Formenti, A. Pazzaglia, F.M. Arioli, A. Tentori, M. Passoni, New J. Phys. **22**, 033045 (2020)

51. D. Jung, B.J. Albright, L. Yin, D.C. Gautier, R. Shah, S. Palaniyappan, S. Letzring, B. Dromey, H.-C. Wu, T. Shimada, R.P. Johnson, M. Roth, J.C. Fernandez, D. Habs, B.M. Hegelich, New J. Phys. **15**, 123035 (2013)